1   **Title:**

2   Enhancing environmental models with a new downscaling method

3   for global radiation in complex terrain

4 **Authors / co authors:**

5 Arsène Druel[1], Julien Ruffault[1], Hendrik Davi[1], André Chanzy[2], Olivier Marloie[1], Miquel De
6 Cáceres[3], Albert Olioso[1], Florent Mouillot[4], Christophe François[5], Kamel Soudani[5], and
7 Nicolas K. Martin-StPaul[1].

8 [1] URFM, INRAE, 84000 Avignon, France; [2] UMR 1114 EMMAH, INRAE, Avignon University,
9 84000 Avignon, France; [3] CREAF, Centre de Recerca Ecològica i Aplicacions Forestals,
10 Bellaterra, Catalonia, Spain; [4] UMR 5175 CEFE, Montpellier University, CNRS, EPHE, IRD,
11 Montpellier, France; [5] UMR 8079 ESE, UPS, CNRS, AgroParisTech, Orsay, France

12 **Correspondence email:** arsene.druel@inrae.fr

13 **Abstract:**

14 Global radiation is a key climate input in forest process-based models (PBM) as it
15 determines photosynthesis, transpiration and the canopy energy balance. While radiation is
16 highly variable at fine spatial resolution in complex terrain due to shadowing effects, data
17 required for PBM currently available over large extents are generally at spatial resolution
18 coarser than ~9 km. Downscaling radiation from large-scale to high resolution available from
19 digital elevation models is therefore of potential importance to refine global radiation
20 estimates and improve PBM estimations. In this study, we introduced a new downscaling
21 model that aims to refine sub-daily global radiation data obtained from climate reanalysis or
22 projection at large scales to the resolution of a given digital elevation model. First,
23 downscaling involves splitting radiation into direct and diffuse fraction. Then, the influence of
24 surrounding mountains' shade on direct radiation and the "bowl" (deep valley) effect (or
25 skyview factor) on diffuse radiation is considered. The model was evaluated by comparing
26 simulated and observed radiation at the Mont Ventoux mountain study site (southeast of
27 France) using the recent ERA5-Land hourly data available at 9 km resolution as input and
28 downscaled at different spatial resolution (from 1 km to 30 m resolution) using a digital
29 elevation model. The downscaling algorithm improved the reliability of radiation at the study
30 site in particular at scales below 150 m. Finally, by using two different process based models
31 (CASTANEA, a process-based model simulating tree growth, and SurEau, a plant-hydraulic
32 model simulating hydraulic failure risk), we showed that accounting for fine resolution
33 radiation can have a great impact on predictions of forest functioning.

34 **Short summary:**

35 Accurate radiation data are essential for the understanding of ecosystem functioning and
36 dynamics. Traditional large-scale data lack the precision needed for complex terrains. This
37 study introduces a new model to enhance radiation data resolution using elevation maps,
38 which accounts for sub-daily direct and diffuse radiation effects caused by terrain features.
39 Tested on a mountainous area, this method significantly improved radiation estimates,
40 benefiting predictions of forest functioning.

1. **INTRODUCTION**

43 Studies assessing the impacts of climate change on forest ecosystem functions increasingly
44 rely on high resolution spatial and temporal climate data. For example, process-based
45 models that aim to evaluate the effect of climate on forest functions and services require
46 daily or sub-daily temporal resolution meteorology as input (*e.g.*, Davi et al., 2006; De
47 Cáceres et al., 2023; Granier et al., 2007; Ruffault et al., 2013, 2022, 2023) to simulate key
48 ecophysiological processes (transpiration, photosynthesis or water potential). Yet, even
49 relatively fine-grained (*i.e.*, 1 km) historical or projected climate products (Hijmans et al.,
50 2005; Brun et al., 2022) do not correspond to the "topographic scale" and cannot reproduce
51 fine-scale patterns observed in heterogeneous landscapes. Moreover, employing spatially-
52 coarse climatic projections can lead to biased and irrelevant inferences of local ecological
53 patterns (Bedia et al., 2013) or to substantial errors in impact studies (e.g., Patsiou et al.,
54 2014; Randin et al., 2009). Improving methodologies to provide climatic data at high spatio-
55 temporal resolution variation is therefore crucial to better understand and predict the spatial
56 heterogeneity in forest structure and functions.

57 Among climate variables, radiation is a key driver of plant functioning and productivity
58 globally (Churkina and Running, 1998), acting through two main mechanisms. On one hand,
59 global radiation determines the photosynthetically active radiation (PAR), *i.e.*, the available
60 energy for photosynthesis and thus plant productivity. Numerous studies have shown the
61 relationship between the amount of solar radiation and the distribution of plant species or
62 communities worldwide (Dirnbock et al., 2003; Franklin, 1998; Meentemeyer et al., 2001;
63 Tappeiner et al., 1998; Zimmermann and Kienast, 1999). On the other hand, the radiation
64 reaching a vegetation surface is an important component of the canopy energy balance,
65 driving surface temperature and vapour pressure deficit (Monteith, 1981). Radiation is thus a
66 key driver of evapotranspiration which enters in most potential evapotranspiration
67 formulations (Fisher et al., 2011) and water balance models (Granier 1999; Ruffault et al.
68 2013; De Cáceres et al., 2015). Through its effect on leaf temperature and vapour pressure
69 deficit, radiation also influences the water status of the leaves which in turn will drive many
70 plant functions including growth, stomatal aperture and desiccation (Martin-StPaul et al.,
71 2023).

72 In regions with a complex orography, climatic variations can occur over distances ranging
73 from a few metres to a few kilometres. This phenomenon, referred to as topoclimate (Bramer
74 et al., 2018), can play a crucial role in shaping flora and fauna habitat as well as a multitude
75 of ecosystem processes related to climatic variability (Austin, 2002; Piedallu & Gégout,

76 2008; Randin et al., 2009). Accounting for topographic effects on spatial radiation patterns
77 has been well studied with the purpose, for instance, of improving niche models (that predict
78 the distribution of plants as a function of environmental variables) in mountainous areas
79 (Piedallu & Gégout, 2008; Randin et al., 2009). So far, such radiation data are measured or
80 computed from local meteorological stations, from coarse-scale global meteorological
81 products such as reanalyses, or geostationary satellite data products at few kilometer
82 resolution (e.g. De Cáceres et al., 2018, Roerink et al. 2012).

83 Direct radiation is a primary driver of topoclimate variations, as it can undergo changes at a
84 very local scale due to several processes. At the scale of a massif, the surrounding
85 topography can cast shadows on a given point because the sun rays can be physically
86 interrupted. In other words, the presence of nearby high peaks will impact the rays directly
87 coming from the sun. At the scale of a point in space, the slope and aspect (azimuth), will in
88 addition modify the direct radiation intensity received. In the northern hemisphere, a south
89 face will receive more radiation than a north face, and this will be modulated by the angle
90 between the sun rays and the slope at the point. Similarly, the surrounding topography will
91 affect diffuse radiation (*e.g.*, on cloudy days) isotropically (at 360°), leading to lower radiation
92 in valley bottoms (*i.e.*, the skyview factor or the "bowl effect").

93 Historically, the primary method for accounting for the effects of topography on radiation has
94 been to rely on slope or aspect. Indeed, these parameters are relatively simple to measure
95 (e.g., through GIS) and the global radiation flux at the surface can be easily derived from
96 those (Austin et al., 1990; Carroll et al., 1999; Clark et al., 1999; Pierce et al., 2005).
97 However, this downscaling approach overlooks a significant portion of the processes
98 involved in radiation attenuation due to sky obstruction by surrounding topography. Shading
99 and the skyview were taken into account at a later stage, in particular in the radiation
100 parameterization scheme (Müller & Scherer, 2005) and in several of its applications (e.g.
101 Senkova et al., 2007; Buzzi, 2008). Regional climate models (RCMs), on the other hand,
102 calculate radiation by accounting for atmospheric processes in relation to land-surface
103 processes (energy balance etc…). Nevertheless, they typically operate on fixed grids,
104 usually at scales of several kilometres (Bailey et al., 2023), which is not precise enough for
105 operational use at point level. More recently, another method employed is statistical
106 downscaling, which is empirical and based on regressions (Davy & Kusch, 2021; Fealy &
107 Sweeney, 2008) or machine learning techniques (Hernanz et al., 2023). However, this
108 requires a lot of field data in different contexts to elaborate an empirical model.

109 Piedallu & Gégout (2008) proposed one method using the slope and the aspect of the point

110 to compute the sun intensity and taking into account the surrounding topography to compute
111 radiation accounting for direct shadowing. They produced a fine scale map (50 * 50 m) over
112 France which is dedicated to statistical niche modelling or mortality risk assessment
113 (Piedallu & Gégout, 2008). However, in the case of process-based vegetation models this
114 has several limitations. Firstly, their approach relies on interpolated meteorological station
115 data to compute the radiation correction at a monthly time step and is thus limited in terms of
116 temporal and spatial accuracy, leading to significant biases in vegetation growth or the
117 smoothing of climatic extremes. Secondly, they do not separate diffuse and direct radiation
118 using clouds but only use an empirical correction of the total radiation using cloud cover.
119 Finally, the skyview factor on diffuse radiation is not taken into account. This method based
120 on measurements is thus limited for projection purposes and requires a large network of
121 equipped stations, resulting in uncertainty. Moreover, it has been applied only to France and
122 has not been generalised to other regions or periods.

123 In this study we present a process-based method to downscale coarse resolution (0.1° at
124 best in general for reanalysis or meteorological models) or geostationary products (2 km
125 resolution at best) global radiation data (such as global reanalysis or climate projections)
126 made on flat surfaces down to the level of 1 km to 30 m resolution Digital Elevation Model
127 (DEM) by accounting for slope, aspect,the shadowing effect on direct radiation and for the
128 skyview factor on diffuse radiation. The method can be applied at any resolution, depending
129 on the choice of the DEM. Moreover, it can be applied to any type of radiation data, making it
130 applicable to any region in the world and to historical periods as well as future projections.
131 The possibility to use reanalyses-derived radiation further ensures physical consistency
132 between the different climate variables used in process-based models. The algorithm was
133 tested on Mont Ventoux and compared with PAR measurements recorded during 2 years at
134 7 sites on this complex topographic area. Finally we evaluated how this new radiation
135 product can impact ecological predictions by simulating the gross primary productivity (GPP)
136 and the risk of drought-induced mortality for the European beech (*Fagus sylvatica)* using two
137 process-based models.

138 **2.** **METHODS**

139 **2.1.** **Radiation downscaling model**
140 The proposed radiation downscaling model aims to refine sub-daily global radiation data
141 obtained from reanalysis at large scales to the resolution of a given DEM. This process-
142 based method can be adapted depending on the input dataset and accounts for the
143 shadowing effect on direct radiation and the skyview factor on diffuse radiation. In order to

ensure its versatility and applicability, we reduced the need for external data that can be challenging to obtain at the local scale, such as cloudiness (Dubayah and Loechel, 1997; Piedallu and Gégout, 2007). The only required input is a DEM whose resolution will determine the final spatial resolution of the radiation data.

Our methodology involves four distinct steps, outlined as follows (see Fig. 1 for visualisation):

i. Splitting direct and diffuse radiation from a large-scale global radiation dataset (optional if the data already contain direct and diffuse radiation).

ii. Downscaling direct radiation by considering local topography and shadowing effects.

iii. Downscaling diffuse radiation by estimating the proportion of diffuse radiation that reaches the target point relative to the surrounding topography.

iv. Summing the downscaled direct and diffuse radiation components.

These steps are described in detail in the subsequent sections.
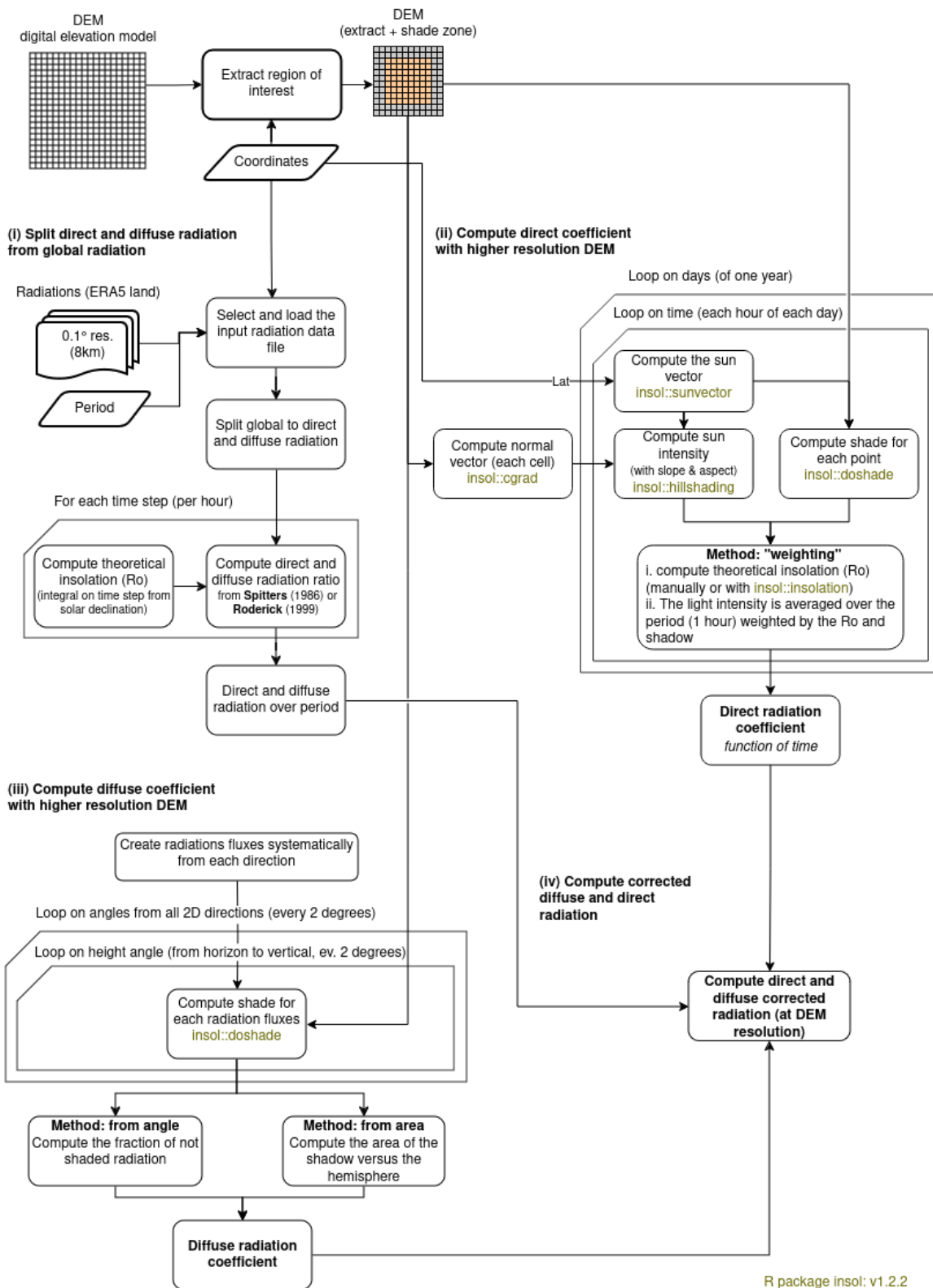
Figure 1: Simplified workflow of radiation downscaling, showing the four different steps of the procedure. The bold boxes at the top left show the data required as inputs (DEM, coordinates, period and large scale radiation), the green boxes show the functions of the external R package used (insol), the truncated boxes show the loops and the rounded boxes show the various stages.

2.1.1. Splitting direct and diffuse radiation

162

163 In cases where only global radiation is available from the input dataset, as in products like

164 ERA5-Land (Muñoz-Sabater et al., 2021), a first step involves extracting hourly direct and

165 diffuse radiation (Fig. 1.i). Various methods exist for this purpose (Oliphant & Stoy, 2018). In

166 this study, we adopted the approach proposed by Spitters et al. (1986). This choice was

167 driven by the relative simplicity of this approach and the fact that it was originally developed

168 for European landscapes. Additionally, we explored other methods, such as the one

169 proposed by Roderick (1999) and the one proposed by Bird and Hulstrom (1981). Results

170 obtained using the Roderick (1999) method align consistently with those presented herein

171 (results not displayed). Unlike the method by Spitters et al. (1986), the method by Bird and

172 Hulstrom (1981) does not rely on global radiation values but instead aims to derive the

173 values of direct and diffuse radiation from theoretical radiation, temperature, humidity,

174 among other factors. However, the outcomes generated by this model significantly deviated

175 from those obtained using the Spitters et al. (1986) method and exhibited inconsistency with

176 available measurements (not shown).

177 The method of Spitters et al. (1986) that was used in this study is an empirical computation

178 technique based on the ratio between theoretical extraterrestrial irradiance (R_0) and the

179 observed value of global radiation (R_g). Specifically, it operates on the assumption that as

180 the ratio of R_g to R_0 decreases, the proportion of diffuse radiation (R_{diff}) relative to direct

181 radiation (R_{dir}) increases - an effect attributed to cloud cover.

182 To compute R_0 (in W.m^{-2}), a common physically-based approach involves using the radiation

183 incident on a plane parallel to the Earth's surface and the sine of solar elevation (which is

184 dependent on latitude and solar time), as follows (Spitters et al., 1986; Widén &

185 Munkhammar, 2019):

$$\text{a.} \quad R_0 = R_{sc}\left[1 + 0.033 \times \cos\left(doy \times 360/365\right)\right] \times \sin\left(\beta\right)$$

186 $$\text{b.} \quad \sin\left(\beta\right) = \sin\left(\lambda\right) \times \sin\left(\delta\right) + \cos\left(\lambda\right) \times \cos\left(\delta\right) \times \cos\left(15 \times \left(t_h - 12\right)\right) \quad (1)$$

$$\text{c.} \quad \delta = \frac{\pi \times 23.45}{180} \times \sin\left(2 \times \pi \times \frac{doy + 284}{365}\right)$$

187 With R_{sc} representing the solar constant (1 361 W.m^{-2}, Coddington et al., 2016), *doy* the day

188 of the year, sin(β) the sine of the solar elevation angle, λ the latitude of the site (in radian), δ

189 the solar declination angle (in degrees) and t_h the hour (in solar time).

190 It's important to note that in this study, global radiation is not treated as a singular value but

191 rather as an average over a short period of time (e.g., between h_t and h_{t+1}, using an hourly

192 time step with ERA5-Land). Thus, *sin(β)* needs to be integrated:

193 $$\int_{h_t}^{h_{t+1}} \sin(\beta) = \sin(\lambda) \times \sin(\delta) +$$ (2)

$$\cos(\lambda) \times \cos(\delta) \times \frac{15 \times \pi}{180} \times \left[\sin\left(\frac{\pi}{180} \times 15 \times (h_{t+1} - 12) \right) - \sin\left(\frac{\pi}{180} \times 15 \times (h_t - 12) \right) \right]$$

194 Then, we used the relationship between the fraction of diffuse radiation (R_{diff}) compared to
195 global radiation data (R_g) and the fraction of global radiation data (R_g) compared to
196 theoretical radiation (R_0), as recommended by de Jon (1980) for hourly radiation (described
197 in Spitters et al., 1986, including values for daily radiation):

198 $\dfrac{R_{diff}}{R_g} = 1$ for $\dfrac{R_g}{R_0} \leq 0.22$

199 $\dfrac{R_{diff}}{R_g} = 1 - 6.4 \times \left(\dfrac{R_g}{R_0} - 0.22 \right)^2$ for $0.22 < \dfrac{R_g}{R_0} \leq 0.35$ (3)

200 $\dfrac{R_{diff}}{R_g} = 1.47 - 1.66 \times \dfrac{R_g}{R_0}$ for $0.35 < \dfrac{R_g}{R_0} \leq K$

201 $\dfrac{R_{diff}}{R_g} = L$ for $K < \dfrac{R_g}{R_0}$

202 With $L = 0.847 - 1.61 \times \sin(\beta) + 1.04 \times \sin^2(\beta)$ and $K = \dfrac{1.47 - L}{1.66}$.

203 Following Spitters et al. (1986), the final step involves subtracting the circumsolar
204 component (R_{circum}) of diffuse radiation from the direct flux: Under clear skies, diffuse
205 irradiance is anisotropic, due to the presence of aerosols in the atmosphere, and the
206 intensity is therefore higher in the direction of the sun. It is thus necessary to attribute the
207 excess diffuse irradiance observed near the direction of global radiation to direct radiation.

208 $R_{circum} = \cos^2\left(\dfrac{\pi}{2} - \beta \right) \times \cos^3(\beta)$ (4)

209 To determine the corresponding fraction of diffuse radiation under intermediate sky
210 conditions, clear to cloudy skies, we adopt the interpolation method introduced by Klucher
211 (1978):

212 $\dfrac{R_{diff}}{R_g} = \dfrac{R_{diff}}{R_g} \div \left[1 + \left(1 - \left(\dfrac{R_{diff}}{R_g} \right)^2 \right) \times R_{circum} \right]$ (5)

213 Finally, considering that global radiation (R_g) comprises the sum of diffuse (R_{diff}) and direct
214 (R_{dir}) radiation components, the value of R_{dir} can be directly inferred from the other two
215 components.

216 **2.1.2. Downscaling direct radiation**

217 To downscale direct radiation (Fig. 1.ii.), two distinct processes were considered. Firstly, the
218 path of sun rays was examined to determine if any obstruction in the topography may block
219 them. Secondly, if unobstructed, the slope and aspect of the pixel are used to compute the
220 radiation intensity relative to a horizontal surface.

221 For both processes, the initial step involved computing the sun vector in three dimensions.
222 This was achieved using the R package "insol" (version 1.2.2, Corripio, 2020) and
223 specifically the "sunvector" function, which defines the vector based on longitude, latitude,
224 and time (day, hour, minute). To assess whether radiation is obstructed by a summit, the
225 close topography derived from a DEM is computed using the "doshade" function within the
226 "insol" package. To determine sun intensity, the "hillshading" function from the same
227 package is utilised, requiring both the sun vector and the topography (previously normalised
228 into unit vectors using the "cgrad" function). Note that the same package is now available for
229 python (on https://pypi.org/project/insolation/ and https://www.meteoexploration.com/insol/).
230 Considering that the input radiation is accumulated over a specific period (e.g., 1 hour in
231 ERA5-Land), and to account for spatial variations in radiation intensity (primarily due to the
232 angle of the sun rays) and shadow projections, several time steps are employed for
233 downscaling the direct radiation. In this study, the default value of three time steps per hour
234 (n = 3) was adopted. Additionally, to aggregate the values while considering temporal
235 variations in radiation intensity, each value is weighted by the theoretical extraterrestrial
236 irradiance (R_0 in Eq. (1)). This yields a corrected direct radiation (R_{dir_cor}):

237 $$R_{dir_{cor}} = R_{dir} \times \frac{\sum_{t_1}^{t_n} \left(R_0 \times S \times \frac{I_{slope}}{I_{vert}} \right)}{\sum_{t_1}^{t_n} R_0}$$ (6)

238 Where S represents the shadow parameter (with a value of 0 indicating shadow and 1
239 indicating no shadow), and I_{slope} and I_{vert} denote the illumination intensity over the slope and a
240 vertical surface, respectively, to derive the relative intensity of sunlight over the slope.

241 ### 2.1.3.   Downscaling diffuse radiation
242 Diffuse radiation is independent of the sun's inclination. It emanates uniformly from all
243 directions within the skydome, limited in this study to the top half-sphere. Therefore, its
244 downscaling (Fig. 1.iii) relies on the surrounding topography in all 360° horizontal directions,
245 particularly the proportion of diffuse radiation from all directions that can reach the point
246 under study.
247 Various methods exist to compute this fraction, including employing numerous random rays
248 or determining, for regular 3D distributed vectors, the level of shadow. In this study, a

249 specific method was devised. It involves computing, for each azimuth angle (with fixed steps

250 of 2°), the minimum unshaded radiation using the "doshade" R function described previously

251 and a DEM.

252 Subsequently, these values are utilised to calculate the shaded area of the top half-sphere

253 and thus the proportion of diffuse radiation reaching the focal point. Finally, this proportion is

254 applied to the diffuse radiation computed in Sect. 2.1.1 to derive the corrected diffuse

255 radiation (R_{diff_cor}).

256 The corrected diffuse and direct radiation can then be directly employed or recombined into

257 corrected global radiation (R_{g_corr}), e.g., to serve as input to a model of forest function or

258 dynamics.

259 ### 2.1.4. Digital elevation model data

260 In various steps of the radiation downscaling, the utilisation of a DEM is imperative (Sect.

261 2.1.2 and 2.1.3). In this study, we evaluated radiation downscaling using different DEMs

262 characterised by varying resolutions.

263 The first dataset is the DEM provided by the Shuttle Radar Topography Mission (SRTM,

264 2013), offering a resolution of 1 arc-second (approximately 30 m). In order to clarify the

265 impact of using different resolutions, the resolution of the SRTM product was downgraded to

266 obtain products with resolutions of 60, 90, 125, 185, 250 and 500 metres using the

267 aggregate function (R, terra 1.7.23 library).

268 An additional series of DEMs was employed: the Global Multi-resolution Terrain Elevation

269 Data 2010 (GMTED2010, Danielson and Gesch, 2011), which encompasses spatial

270 resolutions of 30, 15, and 7.5 arc-seconds, corresponding approximately to resolutions of 1

271 km, 500 m, and 250 m, respectively. These datasets were compiled from diverse sources.

272 However, for the metropolitan France region, the primary source of the dataset was the 1

273 arc-second SRTM DEM.

274 The interest of these DEMs lies in their applicability beyond the geographic scope covered in

275 this study. Their availability at a global terrestrial scale renders them suitable for use in

276 various locations worldwide (with the exception of SRTM, which is limited to latitudes

277 between 60° north and 56° south).

278 ## 2.2. Study area

279 The study area was Mont Ventoux, a mountain located in southeastern France, with its

280 highest point reaching an elevation of 1912 metres (44.174° N - 5.27794° E) (Fig. 2). While

281 Mont Ventoux is predominantly oriented in an east-west direction, it exhibits notable

282 variations in slopes and aspects. The southern flank is characterised by gradual inclines,
283 whereas steeper slopes are evident on its northern side. Mont Ventoux presents a
284 predominantly wooded landscape, featuring a mixed beech-fir forest on its northern side,
285 and a mixed European beech-black pine forest on its southern side, particularly above an
286 elevation of 800 metres (Jean et al., 2023). Below this elevation, the dominant species are
287 more typical of the Mediterranean biome and include coppices of downy oak (*Quercus*
288 *pubescens*), evergreen oak (*Quercus ilex*), Aleppo pine (*Pinus halepensis*) as well as as
289 natural regeneration of Atlas cedar (*Cedrus atlantica*) from old plantation trials of the early
290 20th century.
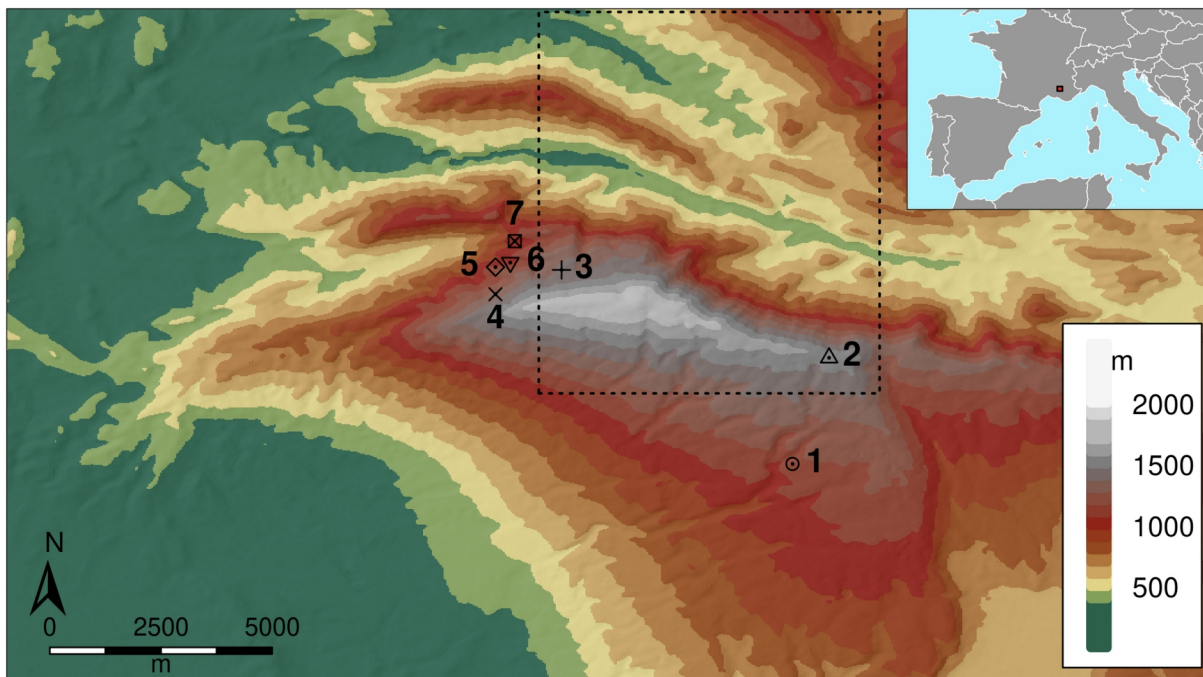
291 **Figure 2: Map of the study area (Mont Ventoux). Mont Ventoux is located in**
292 **southeastern France (see in the inset). Observation points (one symbol with**
293 **associated number) and the ERA5-Land tile (in dotted line) used in this study are**
294 **indicated.**

295 ### 2.3. Global radiation measurements

296 On June, 27 2016, we installed seven mini-weather stations at different strategic elevations
297 and locations on Mont Ventoux (Table 1), each equipped with loggers (YBdesign) and
298 sensors for photosynthetically active radiation (PAR, 400-700 nm), temperature and relative
299 humidity. The sensors were installed on a vertical pole and positioned horizontally (levelled
300 with a spirit level). The PAR sensors (CBE80, brand Solems) and the thermo-hydrometers
301 (EE07-PFT, brand E+E) were calibrated using a reference weather station at the INRAE
302 campus of Avignon before the beginning of the experiment. The mini-weather stations were

positioned in clearings with forest edges extending at a distance minimum of 30 m from the station. The data were recorded at one hour timestep. The photosynthetic flux density delivered by the sensors were converted into $W.m^{-2}$ of global radiation using an empirical relationship calibrated on the ICOS Font-Blanche experimental site (Moreno et al., 2021).

N°	Site	Latitude (°)	Longitude (°)	Elevation (m)	Slope (°)	Aspect(°)
1	Les Tournières	44.129646	5.320524	1159	5.5	250.1
2	Col de la fache	44.157819	5.331975	1575	6.2	201.2
3	Mont Serein	44.182886	5.257725	1413	4.0	234.1
4	dvx5	44.176758	5.238861	1320	20.8	347.2
5	Tc2	44.184014	5.239161	1116	33.1	351.0
6	dvx2	44.185142	5.243383	1074	28.0	355.1
7	142	44.190856	5.244869	1050	23.0	188.4

Table 1. List and main characteristics of the observation sites in Mont Ventoux where radiation measurements were performed. Slope and aspect (azimuth) was computed from a 30 m resolution SRTM digital elevation model.

The observed radiation was compared with the radiation from ERA5-Land before and after downscaling using DEMs at different resolutions. In order to facilitate the comparison between the ERA5-Land reanalysis dataset and observations, which may contain some gaps due to power failure, we aggregated radiation data over various periods (annually or seasonally). This approach involved excluding time steps with missing data, separately for each site. Moreover, to compare with these observations, the correction of the light intensity due to the angle of the direct light rays in relation to the slope and aspect (Sect. 2.1.2, the 'hillshading' function) was deactivated (in Sect. 3.1), as the measurements were carried out on a device placed horizontally.

2.4. Modelling the effect of radiation downscaling on plant functions

To quantify the influence of downscaled radiation on specific applications, we assessed the impact of radiation downscaling on beech (*Fagus sylvatica*) forest functioning using process-based vegetation modelling on the mountainous area of the Mont Ventoux massif (where radiation measurements were located).

We employed two complementary forest vegetation models to quantify how radiation downscaling affects the spatial patterns of both Gross Primary Productivity (GPP) and drought-induced risk of hydraulic failure. These models are, respectively, the forest growth

327 model CASTANEA (Dufrêne et al., 2005) and the plant hydraulic model SurEau (Cochard et
328 al., 2021; Ruffault et al., 2022).

329 CASTANEA is a comprehensive forest soil-vegetation-atmosphere model coupled with a
330 growth module. It simulates carbon (photosynthesis and respiration) and water fluxes
331 (transpiration, soil water content, soil water potential) at a half-hourly to daily time step for an
332 average tree in a homogeneous forest stand. A carbon allocation module assigns a
333 proportion of the daily Net Primary Productivity (NPP) toward various plant compartments
334 (stem, roots, fine roots, flowers, acorn, leaves, and storage) using empirical coefficients.
335 Carbon and water fluxes, including gross and net ecosystem photosynthesis, respiration,
336 transpiration, latent heat fluxes, soil water content, and plant water potential, have been
337 validated on different species and sites, including beech on Mont Ventoux (Davi et al., 2005;
338 Cailleret et al., 2011; Delpierre et al., 2012). In this study, the canopy Gross Primary
339 Productivity (GPP) was used to demonstrate the effects of radiation downscaling on potential
340 productivity.

341 SurEau is a plant-hydraulic model that is dedicated to simulate the risk of drought-induced
342 hydraulic failure due to xylem embolism, a leading mechanism of plant mortality under
343 drought (Cochard et al 2021; Ruffault et al 2022). The model simulates water fluxes and
344 water potential along the soil-plant hydraulic continuum at a half hourly time step, and
345 considers leaf stomata and its regulation, and cuticular transpiration plant organ capacitance
346 an. The model is parameterized with various measurable plant traits previously collected for
347 the target species (Ruffault et al., 2022). In this study, drought-induced risk of hydraulic
348 failure (or the percentage loss of hydraulic conductance) in the vascular system was used as
349 a proxy for hydraulic risk during a given summer.

350 We conducted spatial simulations for one pixel at 0.1° resolution (~ 11 km * 8 km at these
351 coordinates), covering a large part of the Mont Ventoux northern face where the
352 measurements were conducted. The simulations covered the years 2016 and 2017,
353 encompassing the same geographical area as outlined in Sect. 2.3, spanning a segment of
354 Mont Ventoux ranging from 5.25° W to 5.35° W and from 44.15° N to 44.25° N.

355 Climate data were directly sourced from the ERA5-Land hourly dataset (Muñoz-Sabater et
356 al., 2021), including temperature, precipitation, wind speed, relative humidity, and global
357 radiation. The latter was downscaled using the method presented in Sect. 2.1, employing
358 one of the DEMs discussed in Sect. 2.1.4.
359 To maintain consistency and avoid introducing uncertainty from disparate datasets, all other

360 non-climatic inputs were set constant across the study area, as described hereafter. The
361 species selected, *Fagus sylvatica* (European beech), is one of the most common species
362 present on Mont Ventoux (Lander et al., 2021) and its traits are already available for the two
363 models (Cailleret & Davi, 2011; Cailleret et al., 2013; Davi & Cailleret, 2017; Ruffault et al.,
364 2022), with a Leaf Area Index set at 3.5. The soil characteristic corresponded to the median
365 value extracted from the whole studied area from the SoilGrids database (Poggio et al.,
366 2021).

3.   **RESULTS**
367

368   ### 3.1.   **Comparison between simulated and observed global radiation**

369 The comparison of ERA5-Land global radiation, both uncorrected and corrected, with
370 observed global radiation across the 7 studied sites showed the benefit of our downscaling
371 method in accurately estimating local global radiation (Figs. 3, 4 and Table 2).
372 Specifically, the correlation between observed and simulated yearly mean global radiation
373 increased from $r^2 = 0.59$ to $r^2 = 0.93$, while the RMSE decreased from 33.5 to 8.6 $W.m^{-2}$, for
374 the raw ERA5-Land radiation and ERA5-Land radiation corrected with a 30 m resolution
375 DEM, respectively (Fig. 3 and Table 2). However, this increase in the performance of
376 estimating global radiation did not progress consistently as the resolution of our downscaling
377 approach increases. We observed a slight and heterogeneous improvement in the corrected
378 radiation from 1 km to 250 m resolution compared to the raw ERA5-Land resolution (around
379 9 km). It is not until the resolution reaches around 200 metres that a significant and
380 continuous improvement was observed (decrease in RMSE, increase in r^2) until 30 m
381 resolution (Fig. 4).

382 Our results further showed that the absolute performance of radiation models (in terms of r^2)
383 and their relative differences remained consistent across the different studied seasons
384 (Table 2), despite some particularities. During winter, ERA5-Land raw data showed weak
385 correlation with observations (r^2 at 0.37 and RMSE at 38 $W.m^{-2}$), which substantially
386 improved with correction ($r^2 = 0.90$, RMSE = 11 $W.m^{-2}$). Similarly, but more pronounced, in
387 autumn correlations and RMSE were considerably enhanced (respectively r^2 from 0.21 to
388 0.94 and RMSE from 45 to 9 $W.m^{-2}$). In summer, the correlation was almost zero with the
389 ERA5-Land data, whereas it exceeded 0.5 with the corrected radiations. In contrast, the
390 correlation was stable and high (0.85) in spring but did not improve with downscaling, while
391 RMSE improved with correction (35 to 23 $W.m^{-2}$). Further analysis also revealed that the
392 uncorrected (Fig. 3.a) and corrected (Fig. 3.b) seasonal data showed different behavior and

so the equations of the seasonal curves for corrected ERA5-Land radiation closely aligned
with the 1/1 line, in accordance with an important decrease in RMSE. It is noteworthy that
most of the improvement came from points located on northern slopes (points 4, 5 and 6,
Fig. 3). Accordingly, the daily bias from those points was reduced compared to uncorrected
data, while points located on flat surfaces or southern slopes showed low and not significant
bias (not shown).
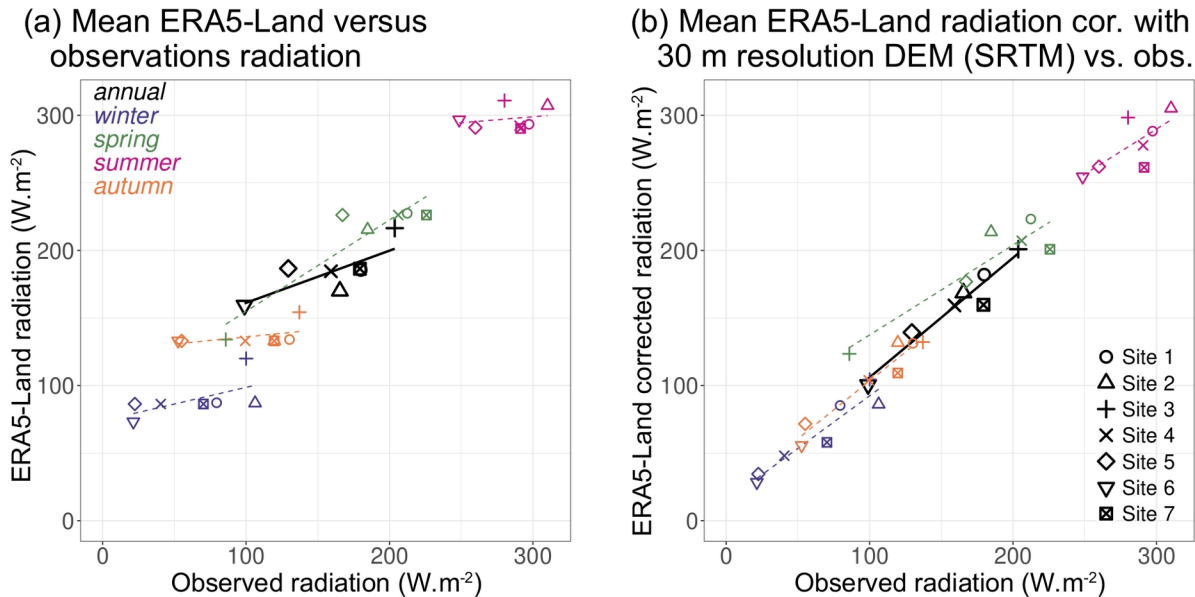
**Figure 3: Comparison of the observed radiation with the ERA5-Land product (a) and
with corrected radiation from ERA5-Land using 30 m resolution DEM (b). For each of
the 7 points studied, the annual (in black) and seasonal (in colours) mean radiation
(W.m^{-2}) are shown, as well as the linear regression line (equation, r^2 and RMSE, see
table 2).**

	ERA5-Land vs. observations			ERA5-Land corrected with 30 m resolution DEM vs. obs.		
	equation	r^2	RMSE	equation	r^2	RMSE
annual	y = 123+ 0.39 x	0.59	33.5	y = 18 + 0.89 x	0.93	8.6
winter	y = 74 + 0.25 x	0.37	37.7	y = 15 + 0.78 x	0.90	11.1
spring	y = 87 + 0.68 x	0.85	35.1	y = 71 + 0.67 x	0.85	22.7
summer	y = 272+ 0.09 x	0.05	24.6	y = 90 + 0.67 x	0.53	14.8
autumn	y = 125+ 0.11 x	0.21	45.3	y = 18 + 0.86 x	0.94	9.1

**Table 2. Linear regression parameters and statistics (r^2 and RMSE, W.m^{-2}) for
comparison of the observed radiation with the ERA5-Land product and with corrected
radiation from ERA5-Land using 30 m DEM (see Fig. 3).**
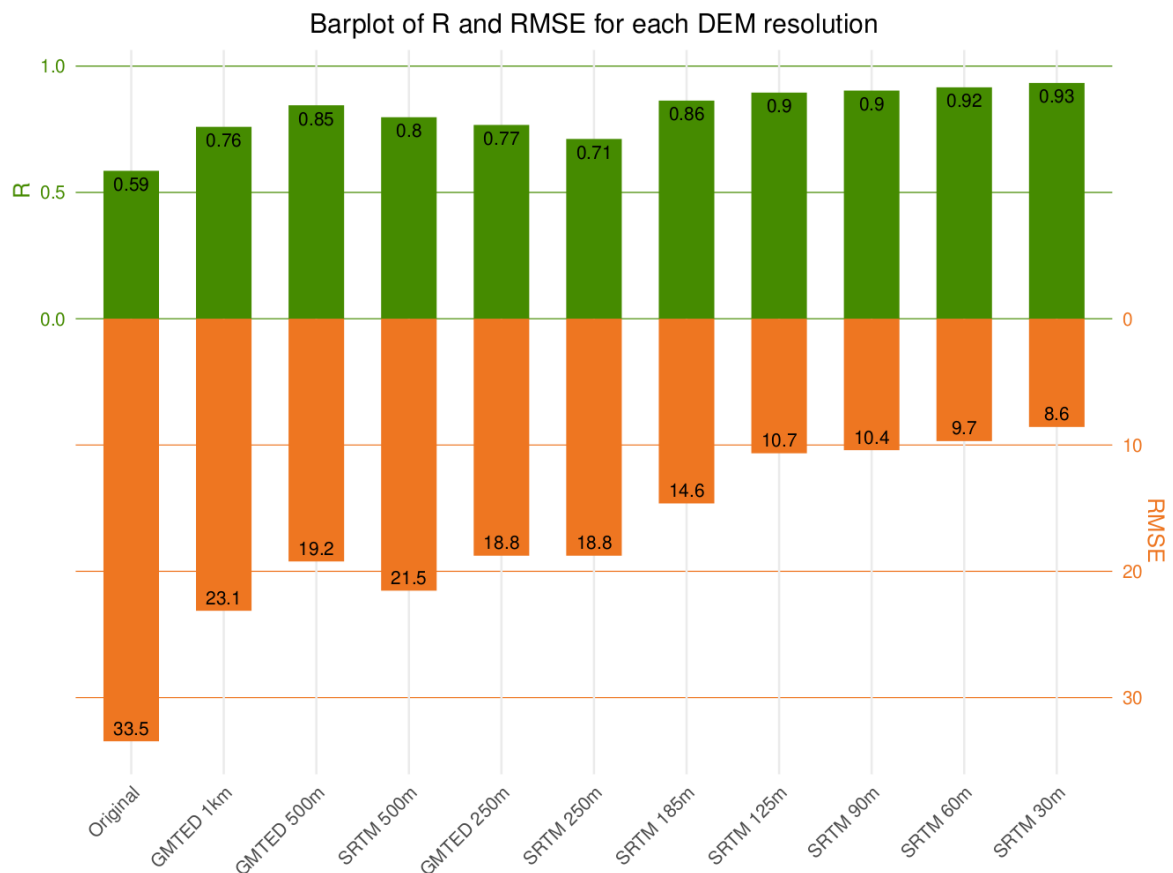
 Figure 4: Comparison of the performances of ERA5-Land product and corrected
radiation from ERA5-Land using different DEMs with observed radiation. The annual
correlation r^2 is represented in green and the RMSE (W.m^{-2}) in orange.

Figure 5 depicts the global radiation values for two distinct sites during two different periods.
Site 1 (refer to Table 1) represents a slightly south-facing location with little shade from
topographical features, particularly evident in winter. Site 5, on the other hand, is situated on
a north-facing slope (slightly west-facing) affecting sunlight exposure, especially during
winter months. Two three-day periods were selected for analysis: one in summer (19-21
August 2016) to observe the impact during peak sun exposure (on the 21st), a cloudy day
(the 20), and an intermediate day (the 19); and another in winter (12 to 14 January 2017,
cloudless days) to assess the effect of the downscaling on low-inclination radiation in a
mountainous region. Three types of radiation values are presented: observed values (Sect.
2.3), original ERA5-Land values (9 km resolution, tile indicated on Fig. 2), and values
following the application of the radiation downscaling with the SRTM DEM (~30 m resolution)
(as described in Sect. 2.1, but without "hillshading" function to be comparable with
measurements which are made with sensors set horizontal). The presence of clouds was
assessed with data combining high-resolution cloud information is directly inferred from

424 satellite observations, such as the Copernicus Atmosphere Monitoring Service (CAMS) solar

425 radiation time-series data (available on

426 https://ads.atmosphere.copernicus.eu/stac-browser/collections/cams-solar-radiation-

427 timeseries, last access the 22/10/2024), and are represented on Fig. S1. The difference

428 between sky-view and all sky radiation indicates the presence of clouds.

429 At site 1 (Fig. 5.a-c), where surrounding topographical features have minimal impact on

430 radiation, the values from ERA5-Land were close to the observations and there was no

431 significant change after radiation downscaling. These trends held for both clear and cloudy

432 days, and for both winter and summer periods. At site 5, disparities between original and

433 corrected ERA5-Land values were more significant due to topographical influences than at

434 site 1. In summer (Fig. 5.b), discrepancies existed between original and corrected ERA5-

435 Land values. Corrected values accurately depict the evolution measured, especially the 21

436 August, and constantly more closely represented measured values, but still struggled to

437 replicate sub-daily variations. Particularly, a dip in the curve around 10am appeared to be

438 present on the 19, possibly indicating a shadow or the presence of localized clouds or fog,

439 but not represented in the original and the corrected radiations. In winter (Fig. 5.d),

440 downscaling markedly impacted radiation values, with corrected values nearly four times

441 lower than ERA5-Land values at the northern site, closely aligning with observed values.

442 Note that if the effect of the slope and aspect on radiation intensity were activated in the

443 script, the effect of the light intensity could increase in the corrected radiation on the south

444 faces, mainly on clear days and in winter (e.g. +10 % for point 1). By contrast it could reduce

445 the corrected radiation on cloud-free days (e.g. by a factor two for 21 August at point 5).
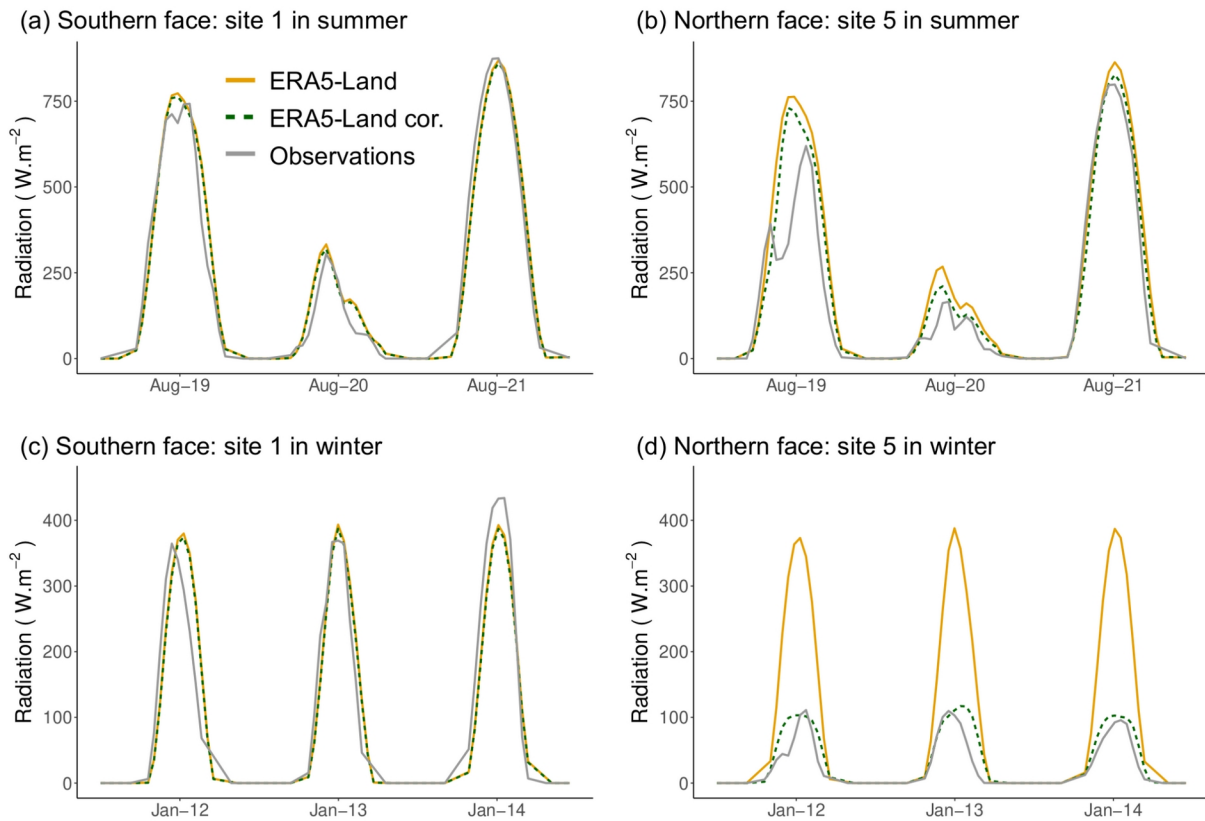
 Figure 5: Radiation of original ERA5-Land data in orange, after downscaling with the
447 SRTM DEM (30 m resolution) in dotted dark green and the observations in grey, for
448 site 1 (a and b) and site 5 (c and d) and for two different dates: one in summer (19-21
449 August 2016 in a and c) and one in winter (12-14 January 2017 in b and d)

450 3.2. Application on Mont Ventoux massif

451 3.2.1. Heterogeneity of global radiation

452 Applying our approach across a heterogeneous geographical area illustrates the spatial and
453 temporal variability in global radiation introduced by downscaling (Fig. 6).

454 Radiation downscaling exerted a clear impact in the mountainous region under study,
455 halving original ERA5-Land global radiation. An evident differentiation emerged between
456 south-facing slopes, which received more radiation, and north-facing slopes, which exhibited
457 minimal radiation levels in winter (approaching zero). Mean radiation values decreased with
458 increasing resolution of the three DEM used, indicating an average decrease of 10.7 % on
459 13 January 2017 and 5.9 % on 19 August 2016 when transitioning from the GMTED DEM at
460 approximately 500 metres to the SRTM at approximately 30 metres resolution. Conversely,
461 standard deviation increased with resolution, rising by 13.5 % and 30.0 %, respectively.
462 During winter, the standard deviation was similar in magnitude of the mean due to low
463 radiation values, whereas in summer, it accounted for 20 to 25 % of the mean.

These differences in standard deviation due to topography implied significant differences between the different DEMs, as well as with the original ERA5-Land values. For instance, the daily accumulation of radiation value recorded on January 13th was 7.3 MJ.m^{-2} in the reanalysis, whereas the maximum daily radiation reached 9.3 MJ.m^{-2} in the ERA5-Land tile with downscaling conducted using the 250 m DEM. Similarly, on January 13th (Fig. 6.b), the spatial pattern representing a denser "line" denoting stronger radiation values around 5.3° E and 44.19° N was relatively narrow with the 30 m DEM (approximately 200 meters wide), whereas it doubled in width with the 500 m DEM.
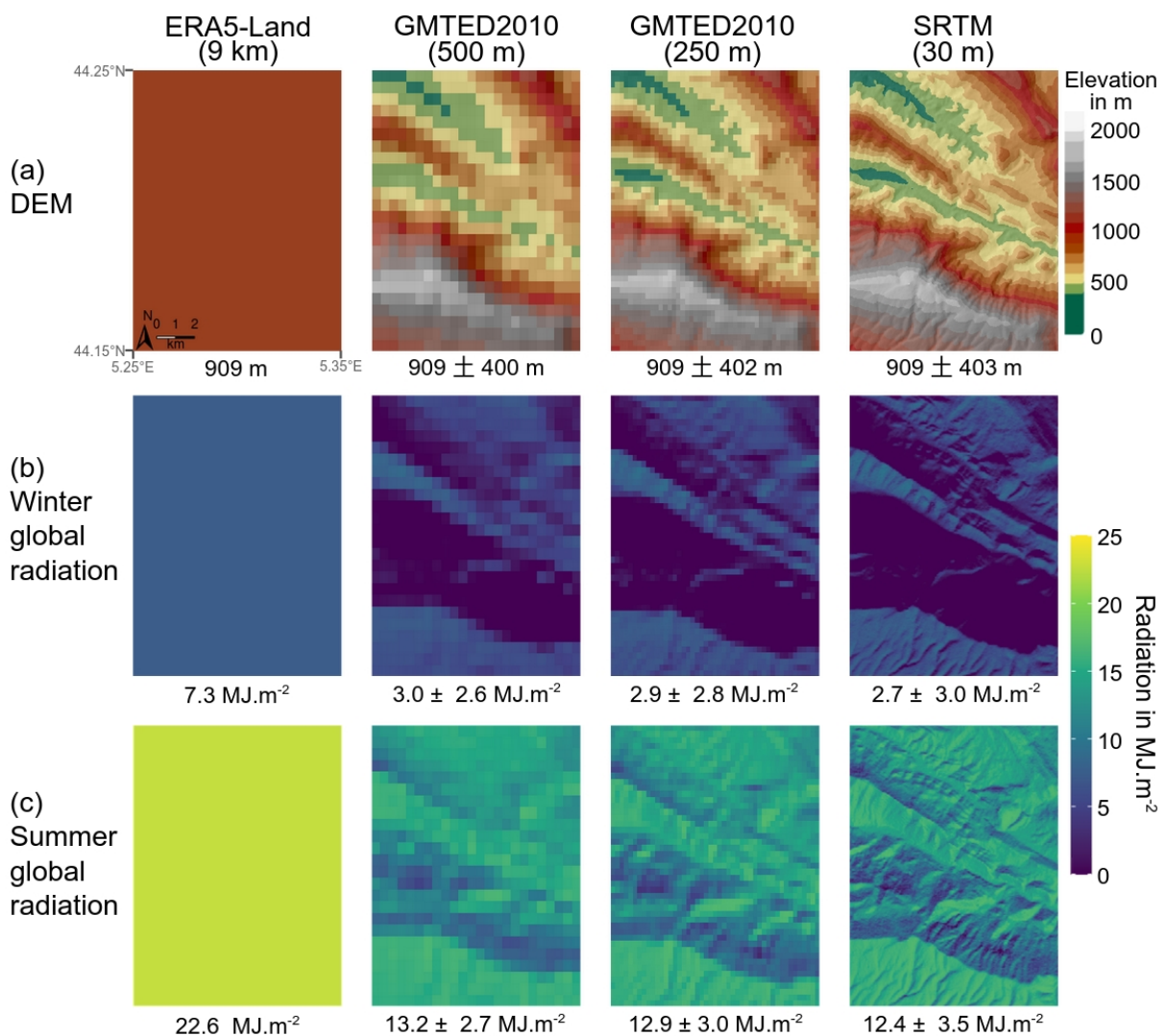
Figure 6: Global radiation from ERA5-Land and resulting from downscaling obtained from different resolution DEMs. (a) ERA5-Land tile (left) and DEM resolution (500, 250, and 30 metres, from left to right). Daily global radiation for two distinct dates, (b) in winter (13 January 2017) and (c) in summer (19 August 2016). Regional mean values and standard deviations are indicated on the bottom of each map.

3.2.2. Modelling the influence of radiation downscaling on vegetation function

Modifying radiation across the entire area according to each DEM had a tangible impact on the predictions of vegetation processes as presented on models output as shown in Fig. 7. In general, the simulations remained consistent across the studied area, despite potential variations introduced by the different topographies used during downscaling. With the three different downscaling (from 8 km to 500 m, 250 m and 30 m), there is a discernible reduction in Gross Primary Productivity (GPP) ranging between 5 % and 8 %, as well as in the risk of hydraulic failure, which decreases between 14 % and 23 %. Moreover, the standard deviation introduced between the values was quite significant, varying between 8 % and 13 % for the two outputs studied.

Upon comparing the patterns obtained with the corresponding DEMs, we observed that south-facing slopes tended to exhibit higher annual productivity (Fig. 7.b) but were susceptible to greater hydraulic stress (as indicated by darker colours in Fig. 7.c). Conversely, north-facing slopes generally manifested lower GPP as simulated by the CASTANEA model, yet exhibited a reduced risk of hydraulic failure.

To evaluate the potential impact of these discrepancies on drought-induced mortality, we computed the risk of hydraulic failure from the SurEau simulations. The relationship between mortality due to water stress and risk of hydraulic failure is often conceptualised as a threshold effect (Choat et al., 2018), although this notion is occasionally questioned (Hammond et al., 2021). Setting at 50% the risk of hydraulic failure threshold at which trees die, we obtained drought-induced mortality percentages in term of surface of 100 %, and 97 %, 98 % and 89 % for the original ERA5-Land tile, and the data downscaled to 500 m, 250 m and 30 m, respectively. Given that the total soil available water accessible for the trees used in this study came from a single value taken from the median over the area of the SoilGrids database (Poggio et al., 2021), and that this value is subject to uncertainty, these results must be compared relatively to each other.
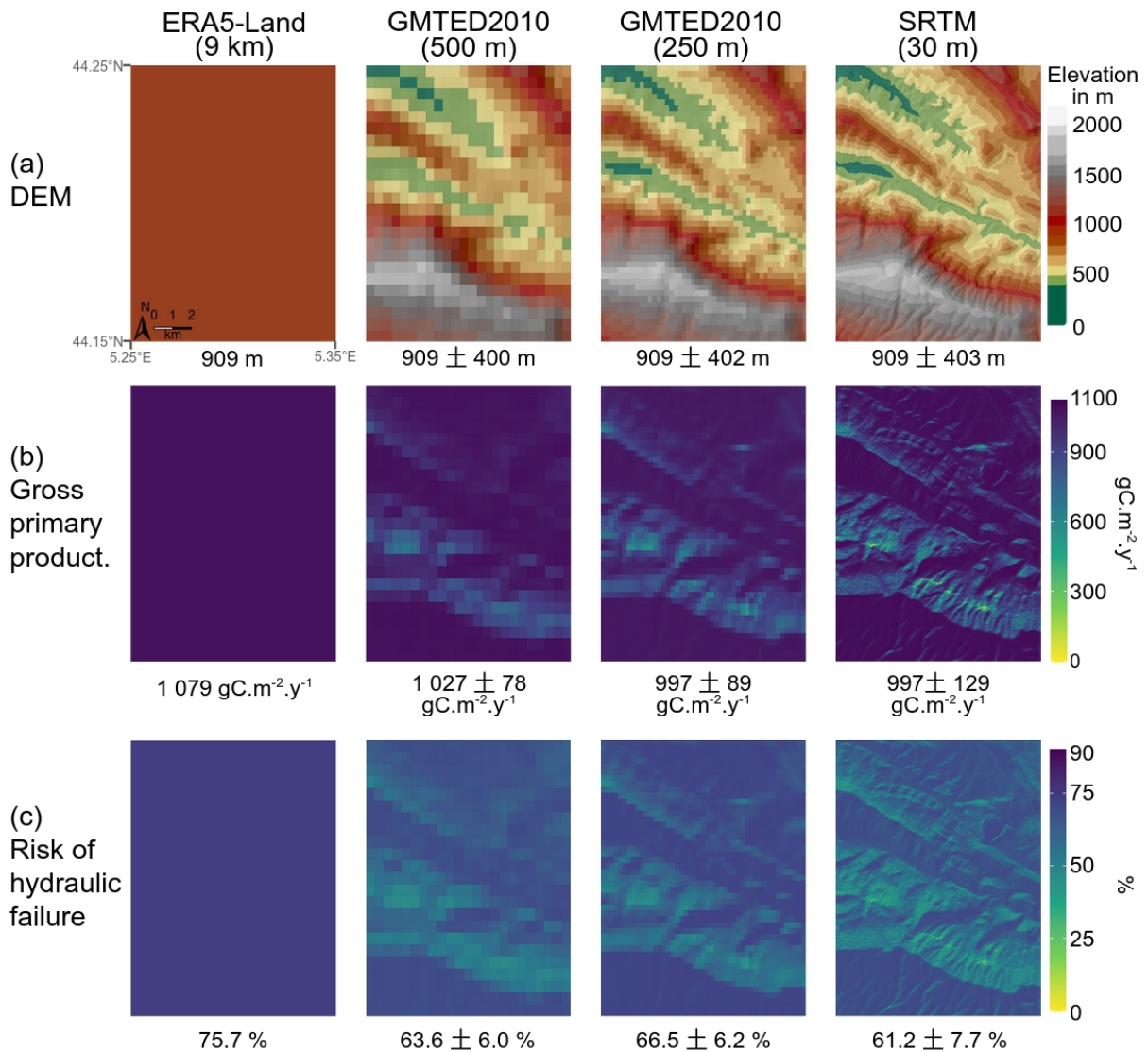
504 **Figure 7: Gross primary productivity and risk of hydraulic failure simulated with,**
505 **respectively, CASTANEA and SurEau, from ERA5-Land and resulting from global**
506 **radiation downscaling obtained from different resolution DEMs. (a) ERA5-Land tile**
507 **(left) and DEM resolution (500, 250, and 30 metres, from left to right). (b) Gross**
508 **primary productivity simulated with CASTANEA. (c) Risk of hydraulic failure**
509 **simulated with SurEau. Regional mean values and standard deviations are indicated**
510 **on the bottom of each map.**

511 ## 4. DISCUSSION

512 ### 4.1. Performance of the downscaling method

513 The radiation downscaling method we present in this study significantly improved radiation
514 predictions in mountainous regions compared to those provided by reanalysis products.
515 More specifically, we demonstrated that accounting for the impact of topography and

516 distinguishing between direct and diffuse radiation allowed us to better capture seasonal
517 radiation patterns. On the north-facing side of our study area, where global radiation is
518 reduced due to the obstruction of direct sunlight by surrounding mountains, our downscaling
519 method significantly lowered radiation levels, particularly during winter when the Sun is at its
520 lowest position on the sky. Conversely, on the south-facing slopes, the steepness of the
521 terrain and the more direct alignment with the sun resulted in increased radiation levels. This
522 effect was also particularly pronounced in winter, when the Sun is lower in the sky but more
523 favourably oriented towards these slopes. Consequently, our method represented the spatial
524 heterogeneity of radiation that can be observed in complex terrain, significantly improving
525 radiation estimations from larger scale renalysis products when a fine downscaling scale is
526 chosen. This corroborates the results reported by other studies based on slope, aspect ratio
527 and skyview, which indicate improved results after downscaling (Müller and Dieter, 2005;
528 Senkova et al., 2007; Buzzi, 2008). Nevertheless, none of these studies combines both high
529 spatial (here ~30 m) and temporal resolution (hourly). Furthermore, by comparing precisely
530 resolved data combining high-resolution cloud information is directly inferred from satellite
531 observations (Fig. S1), the quality of our results is confirmed. While in summer, the CAMS
532 data are consistent with both our results and the observations, in winter the results
533 presented in Fig. 5 are much closer to the observations at the south-facing site, while at the
534 north-facing site the topographical correction allows us to be very close to the observations,
535 whereas the CAMS data are very far from them.

536 Our analysis showed a clear but non-uniform improvement in radiation estimates as the
537 resolution of our downscaling method increased. While no continuous improvement was
538 observed at resolutions coarser than 250 m, a gradual improvement emerged for finer
539 resolutions, down to 30 m. This suggests that topoclimatic processes, such as the effects of
540 topography on local radiation patterns, operate at these finer spatial scales, highlighting the
541 importance of high-resolution estimations for accurately representing the influence of terrain
542 on local climate. On the other hand, our results for resolutions coarser than 250 m, suggest
543 that insufficient improvement in resolution during the downscaling introduces some variance
544 (due to the inherent uncertainty of the method and additional processing of the variable)
545 which can mitigate improvements in radiation representation at the site level.

546 As we clearly observed in our study area, the impact of radiation downscaling was primarily
547 observed in regions with significant shadow casting, whose effect becomes more
548 pronounced as the Sun's zenithal angle decreases. Due to energy equilibrium and
549 conservation at large scale, this implies that an increase in radiation was observed on south-
550 facing slopes or on mountaintops. This effect was particularly pronounced when the angle

between the incoming direct radiation and the aspect of the relief (slope and azimuth) approaches perpendicularity relative to a flat surface. However, it's worth noting that our study area is not characterised by extremely steep mountains, so these effects are primarily observed on moderate slopes. In regions with much steeper terrain, we would expect the impact of topography on radiation to be even more pronounced, especially in valley bottoms, where shading effects could remain significant even on south-facing slopes.

An important source of uncertainty in our radiation downscaling method likely stems from the way global radiation is split into direct and diffuse components using the ratio of R_g to R_0 as a proxy for cloud cover. This approach cannot capture the spatial and temporal heterogeneity of cloud cover, which can be especially significant in mountainous regions (Buzzi, 2008). This explains why, while daily patterns were effectively estimated, sub-daily variations were more difficult to capture. For instance, in Figure 5.b, the dip around 10 a.m. the 19 August may suggest the presence of microclimatic conditions, such as clouds or fog, an effect not considered in our downscaling method. Actually, the original ERA5-Land data cannot depicts the presence of isolated clouds as it happens on the day presented for summer in Figure 5 as they provide averaged values of incoming radiation over the whole mesh area. Such occurrences could be tracked by using higher resolution solar radiation products such as those obtained from satellite imagery and in particular geostationary satellites with a spatial resolution in the order of 2 to 3 km and a time resolution between 5 and 15 minutes (ex. Roerink et al. 2012, Bojanowski et al. 2014).Indeed, this dip may be associated with the presence of small clouds or fog capping Mont Ventoux during morning, signalled by the drop-out between the CAMS clear-sky and all sky (Fig. S1). Similarly, the small dip observed shortly after in Figure 5.a is actually related to the presence of small clouds of fog capping Mont Ventoux during morning, moving from one site to another. Further analyses with such data could help quantify the extent to which this effect contributes to overall uncertainty of our methodology.

4.2. Implications of radiation downscaling for modelling studies and perspectives of improvements

Using downscaled radiation estimations as input in two process-based forest models provides an overview of the impact that radiation downscaling can have on different forest processes, namely Gross Primary Production (GPP) or drought-induced mortality. Overall, our results revealed that the effects of topography on local radiation patterns can have important implications on these key forest processes. For instance, when considering processes that are based on thresholds, such as the drought-induced mortality associated

585 with risk of hydraulic failure, the mortality rate was reduced from 100 % to 89 %. As could be
586 deduced from the results on radiation alone, the impact of downscaling on GPP and drought-
587 induced mortality was most pronounced in areas with significant topographic features, such
588 as north-facing slopes due to shading or south-facing slopes due to increased radiation
589 levels.

590 While the effect of topography on forest ecological processes is often assessed through its
591 impact on temperature or precipitation patterns (Randin et al., 2009), these results suggest
592 that spatial heterogeneity of radiation, through its interaction with topography, seems also
593 crucial for accurately assessing ecological responses and potential threshold effects in
594 complex terrain. Future studies could benefit from integrating our radiation downscaling
595 method to improve predictions of forest functioning at a very local scale.

596 However, these findings should be interpreted with caution as, in our study, only solar
597 radiation was downscaled, leading to potential decoupling with the other forcing variables
598 (temperature, humidity, precipitation and wind). Downscaling methods exist for these
599 variables, for example the use of simple adiabatic gradient for temperature, or kriging
600 methods or high resolution radar data for rainfall (Liston and Elder 2006, Davy & Kusch,
601 2021) or dynamic models (Maraun et al., 2010), but they are not consistent with the one
602 proposed here. We therefore need to check the consistency of each of the downscaling
603 methods, or evaluate if it is possible to integrate this method or its outputs to downscale
604 other variables with other methods. Indeed, it is important to start from physically-consistent
605 data: in this case ERA5-Land, but which can be adapted, as the method can be adapted to
606 any global (or direct and indirect) radiation input. Finally, the method developed here is only
607 applicable to shortwave radiation, which is the only radiation currently required by the
608 models used. Nevertheless, the principle of the method presented here could be used as a
609 starting point for downscaling longwave radiation. Following the principle presented in
610 Senkova et al (2007), the method used for diffuse radiation (based on the skyview) could be
611 partially applicable to longwave radiation. If it is considered as isotropic, incoming
612 atmospheric radiation could be downscaled directly on the basis of the methodology used to
613 downscale diffuse incoming solar radiation. However, it would be necessary to account for
614 the radiation emitted by land surfaces in view as emitted radiation from the surface is usually
615 significantly higher than atmospheric radiation (this would be particularly true for cloudless
616 skies). This would require the knowledge of the surface temperatures of the surrounding
617 areas, but it is also important to recall that the net longwave radiation has a significantly
618 lower impact than the net shortwave radiation on the surface energy balance (ex. Mira et al.
619 2016).

5.   CONCLUSION

620

621 In this study, we developed a process-based method to downscale global radiation data
622 made on flat surfaces, such as coarse spatial resolution global reanalysis data. The method
623 builds upon existing research and goes further than traditional process-based radiation
624 downscaling methods, by accounting for the shadowing effect on direct radiation and for the
625 skyview factor on diffuse radiation (Piedallu & Gégout, 2008). The recent ERA5-Land hourly
626 data available at 9 km resolution was used to compare on Mont Ventoux the impact of
627 radiation downscaling computed from different digital elevation models.

628 The radiation downscaling method effectively captured the overall trend of radiation
629 distribution across mountainous regions. Agreement with observations was improved for
630 downscaled radiation compared to original ERA5-Land data, especially during winter
631 months, due to the higher zenithal angle. This improvement was particularly significant and
632 increased gradually after a certain spatial resolution (~ 150 m). The implications of
633 downscaling for modelling studies was further investigated using two different process-based
634 models representing gross primary productivity and risk of hydraulic failure. The impact of
635 downscaling on those variables was most pronounced in areas with significant topographic
636 features, such as mountainous regions or canyons. Assessing the spatial heterogeneity of
637 radiation, through its interaction with topography, is crucial for accurately addressing
638 ecological responses and potential threshold effects in complex terrain.

639 The method can be applied at any resolution, depending on the choice of the DEM.
640 Moreover, it can be applied to any type of radiation data, making it applicable to any region
641 in the world and to historical periods as well as future projections. Finally, the method could
642 involve other types of climatic data from the same input dataset, such as temperature or
643 precipitation, thereby ensuring physical consistency between the variables. In the future
644 such methods could be included in more generic climate downscaling tools (e.g. Meteoland,
645 De Cáceres et al., 2018) to facilitate the application of process based models at fine
646 resolution.

Code availability

647

648 The scripts corresponding to the method developed in this article is available on GitLab at
649 https://forgemia.inra.fr/urfm/modeldata_toolkit   (commit   afc05ed2)   with   the   prefix
650 "RadDownscaling".
651 The SurEau model code presented in section 2.4 and whose results are presented in section

652 3.2 is available on GitLab at https://forgemia.inra.fr/urfm/sureau (commit ca19abfb), while the
653 CASTANEA version is available on the capsis platform (https://capsis.cirad.fr/, lasted access
654 the 12/06/2024) and can be downloaded from the "download" menu.

655 **Data availability**

656 Data from Mont Ventoux (2016-2017) at the seven sites are provided by URFM-INRAE
657 Avignon. The full dataset and site information can be accessed from
658 https://doi.org/10.57745/B22AUG.
659 DEM data are freely accessible and can be downloaded from https://earthexplorer.usgs.gov/
660 (last accessed 12/06/2024): the Global Multi-resolution Terrain Elevation Data 2010
661 (GMTED2010) (https://doi.org/10.5066/F7J38R2N) and the Shuttle Radar Topography
662 Mission (SRTM) 1 Arc-Second Global (https://doi.org/10.5066/F7PR7TFT).
663 Climate ERA5-Land data (https://doi.org/10.24381/cds.e2161bac), including global radiation,
664 are provided by Copernicus and can be directly downloaded from
665 https://cds.climate.copernicus.eu/cdsapp#!/dataset/reanalysis-era5-land?tab=form   (last
666 accessed 12/06/2024).

667 **Author contribution**

668 Druel, A., Ruffault, J., Davi, H. and Martin-StPaul, N.K. designed the research and
669 performed the research. Druel, A. developed the scripts and the figures. Marloie, O. and
670 Martin-StPaul, N.K. collected the data on Mont Ventoux. Druel, A., Ruffault, J., Davi, H., De
671 Cáceres, M., Mouillot, F., François, C. and Martin-StPaul, N.K. interpreted the results. Druel,
672 A. led the writing of the manuscript with inputs from Ruffault, J., Chanzy, A., Marloie, O., De
673 Cáceres, M., Mouillot, F., François, C., Soudani, K., and Martin-StPaul, N.K. Finally, Druel,
674 A., Ruffault, J., Olioso, A., and Martin-StPaul, N.K., were particularly involved in the review.

675 **Competing interests**

676 The authors declare that they have no conflict of interest.

677 **Acknowledgements**

678 This project received funding from the European Union's Horizon 2020 research and
679 innovation program under Grant Agreement No. 862221 (FORGENIUS). The authors would
680 also like to thank William Brunetto (URFM, INRAE, Avignon, France) for his help with data
681 acquisition on Mont Ventoux and Deborah Verfaillie for her help with proofreading.

References

682 **References**

683   Austin, M.P., Nicholls, A.O. and Margules, C.R.: Measurement of the realised qualitative
684 niche: Environmental niches of five Eucalyptus species. *Ecological Monographs*, 60(2): 161-
685 177, https://doi.org/10.2307/1943043, 1990.

686   Bailey, M. D., Nychka, D., Sengupta, M., Habte, A., Xie, Y., and Bandyopadhyay, S.:
687 Regridding uncertainty for statistical downscaling of solar radiation. *Adv. Stat. Clim.*
688 *Meteorol. Oceanogr.*, 9, 103–120, https://doi.org/10.5194/ascmo-9-103-2023, 2023

689   Bedia, J., Herrera, S. and Gutiérrez, J.M.: Dangers of Using Global Bioclimatic Datasets
690 for Ecological Niche Modeling. Limitations for Future Climate Projections. *Global and*
691 *Planetary Change*, 107, 1-12, http://dx.doi.org/10.1016/j.gloplacha.2013.04.005, 2013.

692   Bird, R. E., and Hulstrom, R. L.: A simplified clear sky model for direct and diffuse
693 insolation on horizontal surfaces. *Solar Energy Research Institute*, TR-642-761, 1981.

694   Bojanowski, J.S., Vrieling, A., and Skidmore, A.K.: A comparison of data sources for
695 creating a long-term time series of daily gridded solar radiation for Europe. *Sol. Energy*, 99,
696 152–171, http://dx.doi.org/10.1016/j.solener.2013.11.007, 2014.

697   Bramer, I., Anderson, B.J., Bennie, J., Bladon, A.J., De Frenne, P., Hemming, D., Hill,
698 R.A., Kearney, M.R., Körner, C.,Korstjens, A.H., Lenoir, J., Maclean, I.M.D., Marsh, C.D.,
699 Morecroft, M.D., Ohlemüller, R., Slater, H.D., Suggitt, A.J., Zellweger, F. and Gillingham,
700 P.K.: Advances in monitoring and modelling climate at ecologically relevant scales.
701 *Advances in Ecological Research*, 58, 101–161.https://doi.org/10.1016/bs.aecr.2017.12.005,
702 2018.

703   Brun, P., Zimmermann, N. E., Hari, C., Pellissier, L. and Karger, D. N.: CHELSA-
704 BIOCLIM+ A novel set of global climate-related predictors at kilometre-resolution. *EnviDat.*,
705 https://www.doi.org/10.16904/envidat.332, 2022.

706   Buzzi, M.: (2008). Challenges in operational numerical weather prediction at high
707 resolution in complex terrain. ETH Zürich, PhD thesis, Veröffentlichung MeteoSchweiz Nr.
708 80, ISSN: 1422-1381, https://doi.org/10.3929/ethz-a-005698833, 2008.

709   Cailleret, M. and Davi, H.: Effects of climate on diameter growth of co-occurring *Fagus*
710 *sylvatica* and *Abies alba* along an altitudinal gradient. *Trees*, 25:265–276.
711 https://doi.org/10.1007/s00468-010-0503-0, 2011.

712   Cailleret M., Nourtier M., Amm A., Durand-Gillmann M. and Davi H.: Drought-induced
713 decline and mortality of silver fir differ among three sites in Southern France. *Annals of*
714 *Forest Science*, 71, 643–657, 2013.

715   Carroll, C., Zielinski, W.J. and Noss, R.F.: Using presence-absence data to build and test
716 spatial habitat models for the Fisher in the Klamath region, U.S.A. *Conservation Biology*,
717 13(6): 1344-1359, https://doi.org/10.1046/j.1523-1739.1999.98364.x, 1999.

718   Clark, D.B., Palmer, M.W. and Clark, D.A.: Edaphic factors and the landscape-scale

719 distributions of tropical rain forest trees. *Ecology*, 80(8): 2662-2675,
720 https://doi.org/10.1890/0012-9658(1999)080[2662:EFATLS]2.0.CO;2, 1999.

721 Choat, B., Brodribb, T. J., Brodersen, C. R., Duursma, R. A., López, R. and Medlyn, B. E.:
722 Triggers of tree mortality under drought. *Nature*, 558(7711), 531–539.
723 https://doi.org/10.1038/s41586-018-0240-x, 2018.

724 Churkina, G., and Running, S. W.: Contrasting Climatic Controls on the Estimated
725 Productivity of Global Terrestrial Biomes. *Ecosystems*, 1(2), 206–215.
726 https://doi.org/10.1007/s100219900016, 1998.

727 Cochard, H., Pimont, F., Ruffault, J. & Martin-StPaul, N.: SurEau: a mechanistic model of
728 plant water relations under extreme drought. *Ann. For. Sci.*, 78,
729 https://doi.org/10.1007/s13595-021-01067-y, 2021.

730 Coddington, O., Lean, J. L., Pilewskie, P., Snow, M. and Lindholm, D.: A Solar Irradiance
731 Climate Data Record. *Bull. Amer. Meteor. Soc.*, 97, 1265–1282,
732 https://doi.org/10.1175/BAMS-D-14-00265.1, 2016.

733 Danielson, J.J., and Gesch, D.B.: Global multi-resolution terrain elevation data 2010
734 (GMTED2010): U.S. Geological Survey Open-File Report 2011–1073, 26 p.,
735 https://doi.org/10.5066/F7J38R2N (Downloaded on https://earthexplorer.usgs.gov/ the 15-
736 10-2021), 2011.

737 Davi, H., Dufrêne, E., Granier, A., Le Dantec, V., Barbaroux, C., François, C. and Bréda,
738 N.: Modelling carbon and water cycles in a beech forest: Part II.: Validation of the main
739 processes from organ to stand scale. *Ecological Modelling*, 185, 387–405.
740 doi:10.1016/j.ecolmodel.2005.01.003, 2005.

741 Davi, H., Dufrêne, E., Francois, C., Le Maire, G., Loustau, D., Bosc, A., Rambal, S.,
742 Granier A. and Moors E.: Sensitivity of water and carbon fluxes to climate changes from
743 1960 to 2100 in European forest ecosystems. *Agric. For. Meteorol.*, 141, 35–56,
744 https://doi.org/10.1016/j.agrformet.2006.09.003, 2006.

745 Davi, H. and Cailleret, M.: Assessing drought-driven mortality trees with physiological
746 process-based models. *Agricultural and Forest Meteorology*, 232, 279–290,
747 https://doi.org/10.1016/j.agrformet.2016.08.019, 2017.

748 Davy, R. and Kusch, E.: Reconciling high resolution climate datasets using KrigR.
749 *Environ. Res. Lett.*, 16, 124040, https://doi.org/10.1088/1748-9326/ac39bf, 2021.

750 De Cáceres, M., Martínez-Vilalta, J., Coll, L., Llorens, P., Casals, P., Poyatos, R.,
751 Pausas, J.G. and Brotons, L.: Coupling a water balance model with forest inventory data to
752 predict drought stress: the role of forest structural changes vs. climate changes. *Agricultural*
753 *and Forest Meteorology*, 213: 77-90, https://doi.org/10.1016/j.agrformet.2015.06.012, 2015.

754 De Cáceres, M., Martin-StPaul, N., Turco, M., Cabon, A. and Granda, V.: Estimating daily
755 meteorological data and downscaling climate models over landscapes. *Environmental*

Modelling and Software, 108: 186-196, doi:10.1016/j.envsoft.2018.08.003, 2018.

De Cáceres M, Molowny-Horas R, Cabon A, Martínez-Vilalta J, Mencuccini M, García-Valdés, R., Nadal-Sala, D., Sabaté, S., Martin-StPaul, N., Morin, X., D'Adamo, F., Batllori, E. and Améztegui, A.: MEDFATE 2.9.3: A trait-enabled model to simulate Mediterranean forest function and dynamics at regional scales. *Geoscientific Model Development*, 16, 3165–3201, https://doi.org/10.5194/gmd-16-3165-2023, 2023.

De Jong, J.B.R.M.: Een karakterisering van de zonnestraling (A characterization of solar radiation) in Nederland. Doctoral report, Eindhoven University of Technology, Netherlands, 97 + 67 pp., 1980.

Delpierre, N., Soudani, K., Franc̦ois, C., Le Maire, G., Bernhofer, C., Kutsch, W., Misson, L., Rambal, S., Vesala, T., and Dufrêne, E.: Quantifying the influence of climate and biological drivers on the interannual variability of carbon exchanges in European forests through process-based modelling. *Agric. For. Meteorol.*, 154–155, 99–112, https://doi.org/10.1016/j.agrformet.2011.10.010, 2012.

Dirnbock, T., Dullinger, S., Gottfried, M., Ginzler, C. and Grabherr, G.: Mapping alpine vegetation based on image analysis, topographic variables and Canonical Correspondance Analysis. *Applied Vegetation Science*, 6: 85-96, https://doi.org/10.1111/j.1654-109X.2003.tb00567.x, 2003.

Dubayah, R. and Loechel, S.: Modeling topographic solar radiation using GOES data. J. *Appl. Meteor.*, 36, 141–154, https://doi.org/10.1175/1520-0450(1997)036<0141:MTSRUG>2.0.CO;2, 1997.

Dufrêne, E., Davi, H., François, C., Maire, G. l., Dantec, V. L., and Granier, A.: Modelling carbon and water cycles in a beech forest: Part I: Model description and uncertainty analysis on modelled NEE. *Ecol. Model.*, 185, 407–436, https://doi.org/10.1016/j.ecolmodel.2005.01.004, 2005.

Fealy, R. and Sweeney, J.: Statistical downscaling of temperature, radiation and potential evapotranspiration to produce a multiple GCM ensemble mean for a selection of sites in Ireland. *Irish Geography*, 41:1, 1-27, DOI: https://doi.org/10.1080/00750770801909235, 2008.

Fisher, J. B., Whittaker, R. J., and Malhi, Y.: ET come home: Potential evapotranspiration in geographical ecology: ET come home. *Global Ecology and Biogeography*, 20(1), 1–18. https://doi.org/10.1111/j.1466-8238.2010.00578.x, 2011.

Franklin, J.: Predicting the distribution of shrub species in southern California from climate and terrain-derived variables. *Journal of Vegetation Science*, 9(5): 733-748, https://doi.org/10.2307/3237291, 1998.

Corripio, J.G.: insol: Solar Radiation. R package version 1.2.2, https://www.meteoexploration.com/R/insol/ (last access 27/05/2024), 2020.

793   Granier, A., Breda, N., Biron, P. and Villette, S.: A lumped water balance model to
794 evaluate duration and intensity of drought constraints in forest stands. *Ecol. Model.*,
795 116:269–283, https://doi.org/10.1016/S0304-3800(98)00205-1, 1999.

796   Granier, A., Reichstein, M., Bréda, N., Janssens, I. A., Falge, E., Ciais, P., Grünwald, T.,
797 Aubinet, M., Berbigier, P., Bernhofer, C., Buchmann, N., Facini, O., Grassi, G., Heinesch, B.,
798 Ilvesniemi, H., Keronen, P., Knohl, A., Köstner, B., Lagergren, F., Lindroth, A., Longdoz, B.,
799 Loustau, D., Mateus, J., Montagnani, L., Nys, C., Moors, E.J., Papale, D., Peiffer, M.,
800 Pilegaard, K., Pita, G., Pumpanen, J., Rambal, S., Rebmann, C., Rodrigues, A., Seufert, G.,
801 Tenhunen, J., Vesala, T. and Wang, Q.: Evidence for soil water control on carbon and water
802 dynamics in European forests during the extremely dry year: 2003. *Agricultural and Forest*
803 *Meteorology*, 143(1-2), 123-145. https://doi.org/10.1016/j.agrformet.2006.12.004, 2007.

804   Hammond, W. M., Yu, K., Wilson, L. A., Will, R. E., Anderegg, W. R. L. and Adams, H. D.:
805 Dead or dying? Quantifying the point of no return from hydraulic failure in drought-induced
806 tree mortality. *New Phytologist*, 223(4), 1834–1843, https://doi.org/10.1111/nph.15922,
807 2019.

808   Hernanz, A., Correa, C., Domínguez, M., Rodríguez-Guisado, E. and Rodríguez-Camino,
809 E.: Comparison of machine learning statistical downscaling and regional climate models for
810 temperature, precipitation, wind speed, humidity and radiation over Europe under present
811 conditions. *International Journal of Climatology*, 43, 13, 6065-6082,
812 https://doi.org/10.1002/joc.8190, 2023.

813   Hijmans, R.J., Cameron, S.E., Parra, J.L., Jones, P.G. and Jarvis, A.: Very high-
814 resolution interpolated climate surfaces for global land areas. *International Journal of*
815 *Climatology*, 25(15):1965-1978, https://doi.org/10.1002/joc.1276, 2005.

816   Jean, F., Davi, H., Oddou-Muratorio, S., Fady, B., Scotti, I., Scotti-Saintagne, C., Ruffault,
817 J., Journe, V., Clastre, P., Marloie, O., Brunetto, W., Correard, M., Gilg, O., Pringarve, M.,
818 Rei, F., Thevenet, J., Turion, N. and Pichot, C.: A 14-year series of leaf phenological data
819 collected for European beech (*Fagus sylvatica L.*) and silver fir (*Abies alba Mill.*) from their
820 geographic range margins in south-eastern France. *Annals of Forest Science*, (2023)80:35,
821 https://doi.org/10.1186/s13595-023-01193-9, 2023.

822   Klein, T.: The variability of stomatal sensitivity to leaf water potential across tree species
823 indicates a continuum between isohydric and anisohydric behaviours. *Funct. Ecol.*, 28,
824 1313–1320, https://doi.org/10.1111/1365-2435.12289, 2014.

825   Klucher, T.M.: Evaluation of models to predict insolation on tilted surfaces. Division of
826 *solar energy,* N.A.S.A. TM-78842, https://doi.org/10.1016/0038-092X(79)90110-5, 1978.

827   Lander, T.A., Klein, E.K., Roig, A. and Oddou-Muratorio, S.: Weak founder effects but
828 significant spatial genetic imprint of recent contraction and expansion of European beech
829 populations. *Heredity (Edinb)*, 126(3):491-504, doi: 10.1038/s41437-020-00387-5, 2021.

Liston, G.E. and Elder, K.: A Meteorological Distribution System for High-Resolution Terrestrial Modeling (MicroMet). *Journal of Hydrometeorology*, 7-2, 217-234, https://doi.org/10.1175/JHM486.1, 2006.

Maraun, D., Wetterhall, F., Ireson, A., Chandler, R., Kendon, E. et al.: Precipitation downscaling under climate change: Recent developments to bridge the gap between dynamical models and the end user. *Reviews of Geophysics*, American Geophysical Union, 48 (3), https://doi.org/10.1029/2009RG000314, 2010.

Martin-StPaul, N., Delzon, S. and Cochard, H.: Plant resistance to drought depends on timely stomatal closure. *Ecology Letters*, 20(11), 1437–1447. https://doi.org/10.1111/ele.1285, 2017.

Martin-StPaul, N., Ruffault, J., Guillemot, J., Barbero, R., Cochard, H., Cailleret, M., Cáceres, M. D., Dupuy, J.-L., Pimont, F., Torres-Ruiz, J. M., and Limousin, J.-M.: How much does VPD drive tree water stress and forest disturbances? *Authorea,* Preprints. https://doi.org/10.22541/au.168147010.01270793/v1, 2023.

Meentemeyer, R.K., Moody, A. and Franklin, J.: Landscape-scale patterns of shrub-species abundance in California chaparral: The role of topographically mediated resource gradients. *Plant Ecology*, 156: 19-41, https://doi.org/10.1023/A:1011944805738, 2001.

Mira, M., Olioso, A., Gallego-Elvira, B., Courault, D., Garrigues, S., Marloie, O., Hagolle, O., Guillevic, P., and Boulet, G.: Uncertainty assessment of surface net radiation derived from Landsat images. *Remote sensing of Environment*, 175, 251–270. http://dx.doi.org/10.1016/j.rse.2015.12.054, 2016.

Monteith, J. L.: Evaporation and surface temperature. *Quarterly Journal of the Royal Meteorological Society*, 107(451), 1–27. https://doi.org/10.1002/qj.49710745102, 1981.

Moreno, M., Simioni, G., Cailleret, M., Ruffault, J., Badel, E., Carrière, S., Davi, H., Gavinet, J., Huc, R., Limousin, J.-M., Marloie, O., Martin, L., Rodríguez-Calcerrada, J., Vennetier, M. and Martin-StPaul, N.: Consistently lower sap velocity and growth over nine years of rainfall exclusion in a Mediterranean mixed pine-oak forest. *Agricultural and Forest Meteorology*, 308–309, 108472. https://doi.org/10.1016/j.agrformet.2021.108472, 2021.

Müller, M. D. and Scherer, D.: A grid- and subgrid-scale radiation parametrization of topographic effects for mesoscale weather forecast models. *Monthly Weather Review*, 133, 1431–1442, https://doi.org/10.1175/MWR2927.1, 2005.

Muñoz-Sabater, J., Dutra, E., Agustí-Panareda, A., Albergel, C., Arduini, G., Balsamo, G., Boussetta, S., Choulga, M., Harrigan, S., Hersbach, H., Martens, B., Miralles, D. G., Piles, M., Rodríguez-Fernández, N. J., Zsoter, E., Buontempo, C., and Thépaut, J.-N.: ERA5-Land: a state-of-the-art global reanalysis dataset for land applications. *Earth Syst. Sci. Data*, 13, 4349–4383, https://doi.org/10.5194/essd-13-4349-2021, 2021.

Oliphant, A. J., & Stoy, P. C.: An evaluation of semiempirical models for partitioning

867 photosynthetically active radiation into diffuse and direct beam components. Journal of
868 GeophysicalResearch: *Biogeosciences*, 123, 889–901,
869 https://doi.org/10.1002/2017JG004370, 2018.

870 Patsiou, T.S., Conti, E., Zimmermann, N.E., Theodoridis, S. and Randin, C.F.: Topo-
871 climatic microrefugia explain the persistence of a rare endemic plant in the Alps during the
872 last 21 millennia. *Global Change Biology*, 20(7):2286–2300,
873 https://doi.org/10.1111/gcb.12515, 2014.

874 Piedallu, C. and Gégout, J.-C.: Multiscale computation of solar radiation for predictive
875 vegetation modelling. *Ann. For. Sci.*, 64, 899-909, DOI: 10.1051/forest:2007072, 2007.

876 Piedallu, C. and Gégout, J-C.: Efficient assessment of topographic solar radiation to
877 improve plant distribution models. *Agricultural and Forest Meteorology*, 148 (11), pp.1696-
878 1706., https://doi.org/10.1016/j.agrformet.2008.06.001, 2008.

879 Pierce, K.B., Lookingbill, T. and Urban, D.: A simple method for estimating potential
880 relative radiation (PRR) for landscape-scale vegetation analysis. *Landscape Ecology*, 20(2):
881 137-147, https://doi.org/10.1007/s10980-004-1296-6, 2005.

882 Poggio, L., De Sousa, L. M., Batjes, N. H., Heuvelink, G. B. M., Kempen, B., Ribeiro, E.,
883 and Rossiter, D.: SoilGrids 2.0: Producing soil information for the globe with quantified
884 spatial uncertainty. *Soil*, 7(1), 217–240. doi: 10.5194/soil-7-217-2021, 2021.

885 Randin, C. F., Engler, R., Normand, S., Zappa, M., Zimmermann, N. E., Pearman, P. B.,
886 Vittoz, P., Thuiller, W. and Guisan, A.: Climate change and plant distribution: local models
887 predict high-elevation persistence. *Global Change Biology*, 15(6), 1557-1569.
888 https://doi.org/10.1111/j.1365-2486.2008.01766.x, 2009.

889 Roderick, M. L.: Estimating the diffuse component from daily and monthly measurements
890 of global radiation. *Agricultural and Forest Meteorology*, 95, 169-185,
891 https://doi.org/10.1016/S0168-1923(99)00028-3, 1999.

892 Roerink, G.J., Bojanowski, J.S., de Wit, A.J.W., Eerens, H., Supit, I., Leo, O. and
893 Boogaard, H.L.: Evaluation of MSG-derived global radiation estimates for application in a
894 regional crop model. *Agric. For. Meteorol.*, 160, 36-47,
895 https://doi.org/10.1016/j.agrformet.2012.02.006, 2012.

896 Ruffault, J., Martin-StPaul, N.K., Rambal, S. et Mouillot, F.: Differential regional
897 responses in drought length, intensity and timing to recent climate changes in a
898 Mediterranean forested ecosystem. *Climatic Change*, 117, 103–117,
899 https://doi.org/10.1007/s10584-012-0559-5, 2013.

900 Ruffault, J., Pimont, F., Cochard, H., Dupuy, J.-L., and Martin-StPaul, N.: SurEau-Ecos
901 v2.0: a trait-based plant hydraulics model for simulations of plant water status and drought-
902 induced mortality at the ecosystem level, *Geosci. Model Dev.*, 15, 5593–5626,
903 https://doi.org/10.5194/gmd-15-5593-2022, 2022.

904 Ruffault, J., Limousin, J-.M., Pimont, F., Dupuy, J-.L., De Cáceres, M., Cochard, H.,
905 Mouillot, F., Blackman, C.J., Torres-Ruiz, J.M., Parsons, R.A., Moreno, M., Delzon, S.,
906 Jansen, S., Olioso, A., Choat, B. and Martin-StPaul, N.: Plant hydraulic modelling of leaf and
907 canopy fuel moisture content reveals increasing vulnerability of a Mediterranean forest to
908 wildfires under extreme drought. *New Phytologist*, 237, 4, 1256-1269,
909 https://doi.org/10.1111/nph.18614, 2023.

910 Senkova, A. V., Rontu, L., and Savijärvi, H.: Parametrization of orographic effects on
911 surface radiation in HIRLAM. *Tellus A: Dynamic Meteorology and Oceanography*, 59:3, 279-
912 291, https://doi.org/10.1111/j.1600-0870.2007.00235.x, 2007

913 Spitters, C.J.T., Toussaint, H.A.J.M., and Goudriaan, J.: Separating the diffuse and direct
914 component of global radiation and its implications for modeling canopy photosynthesis Part I.
915 Components of incoming radiation. *Agr. and Forest Met.*, 38(1-3), 217-229,
916 https://doi.org/10.1016/0168-1923(86)90060-2, 1986.

917 Shuttle Radar Topography Mission (SRTM): 1 Arc-Second Global (2013).
918 https://doi.org/10.5066/F7PR7TFT (Downloaded on https://earthexplorer.usgs.gov/ the 15-
919 10-2021), 2013.

920 Stéfanon, M., Martin-StPaul, N. K., Leadley, P., Bastin, S., Dell'Aquila, A., Drobinski, P.,
921 and Gallardo, C.: Testing climate models using an impact model: What are the advantages?
922 *Climatic Change*, 131(4), 649–661, https://doi.org/10.1007/s10584-015-1412-4, 2015.

923 Tappeiner, U., Tasser, E. and Tappeiner, G.: Modelling vegetation patterns using natural
924 and anthropogenic influence factors: preliminary experience with a GIS based model applied
925 to an Alpine area. *Ecological Modelling*, 113(1-3): 225-237, https://doi.org/10.1016/S0304-
926 3800(98)00145-8, 1998.

927 Widén, J. and Munkhammar, J.: Solar Radiation Theory. *Uppsala University, Department
928 of Engineering Sciences*, https://doi.org/10.33063/diva-381852, 2019.

929 Zimmermann, N.E. and Kienast, F.: Predictive mapping of alpine grasslands in
930 Switzerland: Species versus community approach. *Journal of Vegetation Science*, 10(4):
931 469-482, https://doi.org/10.2307/3237182, 1999.